





Combining steady-state with frequency and time domain data to quantitatively analyze charge transport in organic light-emitting diodes F

Cite as: J. Appl. Phys. **127**, 031102 (2020); <https://doi.org/10.1063/1.5132599>

Submitted: 22 October 2019 . Accepted: 05 January 2020 . Published Online: 17 January 2020

S. Jenatsch , S. Züfle , B. Blülle , and B. Ruhstaller 

COLLECTIONS

F This paper was selected as Featured



View Online



Export Citation



CrossMark

ARTICLES YOU MAY BE INTERESTED IN

[Thin film metallic glasses: Properties, applications and future](#)

Journal of Applied Physics **127**, 030901 (2020); <https://doi.org/10.1063/1.5122884>

[Quantitative thermal measurement by the use of scanning thermal microscope and resistive thermal probes](#)

Journal of Applied Physics **127**, 031103 (2020); <https://doi.org/10.1063/1.5125062>

[Uni-traveling-carrier photodiodes](#)

Journal of Applied Physics **127**, 031101 (2020); <https://doi.org/10.1063/1.5128444>

Lock-in Amplifiers
Find out more today



Zurich Instruments



Combining steady-state with frequency and time domain data to quantitatively analyze charge transport in organic light-emitting diodes

Cite as: J. Appl. Phys. **127**, 031102 (2020); doi: [10.1063/1.5132599](https://doi.org/10.1063/1.5132599)

Submitted: 22 October 2019 · Accepted: 5 January 2020 ·

Published Online: 17 January 2020



View Online



Export Citation



CrossMark

S. Jenatsch,^{1,a)}  S. Züfle,^{1,2}  B. Blülle,¹  and B. Ruhstaller^{1,2} 

AFFILIATIONS

¹Fluxim AG, Katharina-Sulzer-Platz 2, 8400 Winterthur, Switzerland

²Institute of Computational Physics, Zurich University of Applied Sciences, Wildbachstrasse 21, 8401 Winterthur, Switzerland

^{a)}Author to whom correspondence should be addressed: sandra.jenatsch@fluxim.com

ABSTRACT

Typically, organic light-emitting diodes (OLEDs) are characterized only in steady-state to determine and optimize their efficiency. Adding further electro-optical measurement techniques in frequency and time domain helps to analyze charge carrier and exciton dynamics and provides deeper insights into the device physics. We, therefore, first present an overview of frequently used OLED measurement techniques and analytical models. A multilayer OLED with a sky-blue thermally activated delayed fluorescent dopant material is employed in this study without loss of generality. Combining the measurements with a full device simulation allows one to determine specific material parameters such as the charge carrier mobilities of all the layers. The main part of this tutorial focuses on how to systematically fit the measured OLED characteristics with microscopic device simulations based on a charge drift-diffusion and exciton migration model in 1D. Finally, we analyze the correlation and sensitivity of the determined material parameters and use the obtained device model to understand limitations of the specific OLED device.

© 2020 Author(s). All article content, except where otherwise noted, is licensed under a Creative Commons Attribution (CC BY) license (<http://creativecommons.org/licenses/by/4.0/>). <https://doi.org/10.1063/1.5132599>

I. INTRODUCTION

The newest display technologies could not be realized without developments in organic light-emitting diodes (OLEDs). Despite their commercial success, there are still issues regarding efficiency and lifetime of these devices to bring the technology to the next level. Especially, the blue emission color is currently lagging behind the performance and reliability of the green and red pixels, which affects the overall display operation, pixel layout choice, and performance.¹ It is, therefore, extremely important to better understand the device physics in general and the origins of degradation in these OLED devices, in particular. Novel insight into the operating mechanisms will allow for the design and selection of new materials or provide guidance to optimize the device structure.

Besides the traditional solution or film characterization techniques, such as cyclic voltammetry^{2–4} and ultraviolet photoelectron spectroscopy (UPS),⁵ new materials need to be thoroughly characterized in full multilayer OLED devices or specific layer stacks to

assess their suitability in real applications. This is also important as material properties may depend on the device fabrication details as well as the specific layer sequence.^{6–10} Thus, reliable material characterization in complete OLED devices is a key requirement. Yet, material parameters are traditionally still extracted from single measurements on specific samples even if analytical models are insufficient. This approach is time-consuming and requires high material consumption, and the determined parameters are of limited validity because they might depend on the explicit device structure or on some measurement parameters.^{11–13}

The preferred way to determine material parameters in complete OLED devices is, therefore, to combine numerical simulations with experimental data. Often, these comparisons were solely focusing on steady-state analysis.^{14–16} In such cases, care has to be taken about the correlation between and the sensitivity to the analyzed material parameters.^{17–19} In order to increase the reliability of device simulation, it is inevitable to include complementary measurement techniques in time and/or frequency domain.^{19–21}

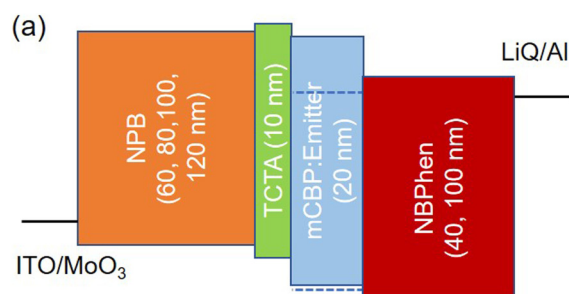
In this tutorial article, we will first describe various commonly used electro-optical measurement techniques for OLED devices. The main part consists of a specific example showing in detail how the obtained measurements of a sky-blue OLED can be fitted with microscopic device simulations. During the fitting procedure, we demonstrate the importance of including complementary measurement techniques and devices with systematically varied thicknesses. In the last part, we demonstrate how the simulation can further be used to analyze device characteristics and how possible routes for efficiency improvements can be identified based on these findings.

II. BACKGROUND

In this section, we will introduce the studied OLED structure and all the measurement techniques that were used. The simulation model and the required input parameters are described in Sec. II C, while the applied workflow is summarized in Sec. II D.

A. Sample design

The employed OLED structure is illustrated in Fig. 1. The layer sequence and the sky-blue emitter is similar to the one described by Peng *et al.*²² and represents a prototypical OLED structure that is frequently used in academic and industrial research studies. The well-known materials NPB [*N,N'*-di(1-naphthyl)-*N,N'*-diphenyl-(1,1'-biphenyl)-4,4'-diamine] and TCTA [tris(4-(9H-carbazol-9-yl)phenyl)amine] are used as hole transport and exciton blocking materials, respectively. The emitter exhibits thermally activated delayed fluorescent (TADF) properties and is blended into the mCBP [3,3'-di(9H-carbazol-9-yl)-1,1'-biphenyl] host with a concentration of 20 vol. %. Here, we investigate a systematic thickness



(b)

NPB \ NBPhen	60 nm	80 nm	100 nm	120 nm
40 nm	S12	S22	S32	S42
100 nm	S11	S21	S31	S41

FIG. 1. (a) Sketch of the employed device structure. (b) The NPB and NBPhen layers are varied in thickness. The devices are labeled according to these layer thicknesses.

variation of the hole transport layer NPB as well as of the electron transport layer NBPhen [2,9-di(naphthalen-2-yl)-4,7-diphenyl-1,10-phenanthroline]. Among others, this variation allows us to determine the relative permittivity of the NPB and the NBPhen layers directly from the measured device capacitance (see Sec. III A).

B. Measurement techniques

In this section, the relevant measurement techniques applied to the batch of OLEDs are explained. Additionally, some common analysis methods are described. For the sake of data comparability, it is crucial that all measurements are consistent, and that systematic uncertainties introduced by individual measurement setups for each technique can be excluded. In the present study, this consistency is ensured by using the all-in-one measurement platform Paios, which sequentially measures all electrical characteristics of one or several devices without the need to change the contact or the measurement system.²³ In this way, any potential degradation between the different measurements can be reduced to a minimum or even completely excluded.

1. Current-voltage-luminance

The current-voltage-luminance (IVL) measurement is the basic characterization method for OLEDs. Here, the pulsed mode is used. This means that we apply a certain voltage V_{app} for 80 ms and subsequently switch back to 0 V before moving to the next voltage point. The current (luminance) at V_{app} is averaged between 20 and 80 ms, and the current (luminance) at 0 V is subtracted. Compared to the staircase (sequential) voltage scan, this method ensures reduced self-heating of the OLED device and, thus, allows to go to higher current densities. Moreover, we can compensate for unintentional background light or for electrical noise in the light detection system.

This steady-state characterization is used to quantify the luminance efficiency, current efficacy, or external quantum efficiency (EQE). Another interesting parameter that can directly be read from the measurement is the onset voltage (V_{onset}). In case of sufficient bipolar injection, the onset is usually related to the bandgap of the emitting layer (EML).²⁴ The obtained *IV* measurement can also be fitted by a single diode model to yield series R_s and parallel resistance R_p as well as reverse saturation current I_0 and dark ideality factor n .¹⁷

2. Impedance spectroscopy

Impedance spectroscopy (IS) is often employed to study device properties of organic single-carrier devices,^{19,25} solar cells,^{17,26–28} and OLEDs.^{21,29,30} A voltage signal consisting of a steady-state bias V_{DC} and an oscillating V_{AC} part is applied to the device. The oscillating current I_{AC} is measured, and the resulting complex admittance Y (impedance Z) is calculated according to

$$\bar{Y} = \frac{1}{Z} = \frac{I_{AC}}{V_{AC}} = G + i2\pi fC. \quad (1)$$

The representation of the IS data can vary. Typically, the conductance G and the capacitance C are evaluated from the real and

imaginary parts of the admittance, respectively. Either the steady-state voltage V_{DC} is varied at a fixed frequency f or the frequency is varied at a constant V_{DC} . Here, we evaluate capacitance- (C - f) and conductance-frequency (G - f) plots at different V_{DC} . The amplitude of the oscillating voltage was always 70 mV. The benefit of considering the capacitance is that for interpretation of the data it can be related to the geometrical capacitance of the device and to parallel plate capacitances of individual layers or set of layers. Another popular representation is the use of real and imaginary parts of the impedance Z .

Moreover, the capacitive response can, for instance, be used to determine the relative permittivity of the organic materials, assuming the OLED to be well represented by a parallel plate capacitor. In specific cases, there are analytical formulas that can be used to determine the charge carrier mobility.^{19,31} Qualitatively, impedance data can also be used to investigate charge carrier injection, accumulation, and trap states.^{17,19,21,25,26,29–33} Often, the impedance measurements are fitted by equivalent circuits.^{28,29,34,35} In order to gain some knowledge on the operation principle of the investigated device, the individual elements of the electrical circuit have to be assigned to different layers and physical processes. Depending on the complexity of the chosen equivalent circuit, this assignment can be ambiguous. Reliable material parameter extraction is, therefore, challenging.

3. Transient electroluminescence

For a transient electroluminescence (TEL) measurement, a rectangular voltage pulse V is applied to the OLED device with varied amplitude. The length of the pulse is chosen such that steady-state conditions are reached at the end of the pulse. Both the rise of the luminance signal as well as the decay can provide valuable insight into charge carrier and exciton dynamics in the OLED.

The measured characteristic onset time in the TEL signal can be related to the transit time t_{tr} , i.e., the time it takes for the charge carriers to be injected and transported before meeting and recombining radiatively. Thus, the onset time directly reflects the two charge carrier mobilities of electrons and holes. An analytical relation between the transit time t_{tr} and the charge carrier mobility μ is given by³⁶

$$\mu = \frac{d^2}{t_{tr}(V - V_{bi})}, \quad (2)$$

where d is the thickness of the device and V_{bi} is the built-in potential. Usually, the transit time is approximated by the delay time t_d between the voltage turn-on and the light onset, which might lead to an overestimation of the mobility.³⁶ This simple formula was developed for single-layer devices that are not injection limited and neglects the spatial variation of the electric field due to the accumulated charge.^{36–38} In multilayer bipolar devices, the relevant thickness parameter d corresponds to the distance which the slower charge carrier needs to travel in order to meet and recombine with the counter-charge. Even though in state-of-the-art OLEDs, the onset analysis only yields an apparent mobility, the technique can nevertheless be very useful to qualitatively understand basic charge transport phenomena.³⁹ The analysis of the TEL rise dynamics is not

discussed here in detail for sake of brevity, even though fast and subsequent slow rise can be assigned to two carriers in the emission layer³⁶ and sometimes a TEL onset overshoot can be observed due to rapid depletion of internally accumulated charges.⁴⁰

The TEL decay, however, is generally related to exciton dynamics and interpreted similarly to transient photoluminescence (TRPL). A single exponential decay fit yields an exciton lifetime that can be related to the radiative and non-radiative recombination rates. In contrast to TRPL, also charge carriers are present in a TEL experiment. Therefore, the decay can be affected by exciton-polaron interactions⁴¹ and delayed recombination of charge carriers.²⁰ Such TEL data have been analyzed in depth to understand different losses in OLED devices^{20,42,43} as well as changes during device degradation.⁴⁴

4. Injection-CELIV

Charge extraction by linearly increasing voltage (CELIV) has first been presented as an analysis technique for inorganic solar cell devices.^{45,46} In this experiment, mobile charge carriers that are present in the device are extracted by a reverse voltage ramp (triangular pulse). The associated current is composed of a constant displacement current and an overshoot that is related to the extracted charge carriers. Depending on the way that charge carriers are generated inside the device, one can distinguish between dark- (doping), photo- (light pulse), and injection-CELIV (offset voltage). While the second is commonly used for organic solar cells,^{11,13,26,47,48} the last is mostly employed in metal-insulator-semiconductor (MIS) devices as well as in OLEDs.^{30,49,50}

In all CELIV techniques, the characteristic current peak area, namely, the time integral of the current overshoot, can be analyzed to estimate the amount of accumulated charge in the device. The peak time t_{max} is related to the charge carrier mobility μ following the analytically derived formula:

$$\mu = \frac{2d^2}{3At_{max}^2}, \quad (3)$$

where d is the thickness of the device and A is the employed voltage ramp. Several modifications of this formula have been presented to account for commonly neglected effects such as the non-uniform field and charge distribution, series resistance, and recombination.^{51–56} As for the TEL rise, the use of multilayer OLED structures complicates or even excludes the application of the analytical formula to extract charge carrier mobilities accurately and assigns the mobility value to a specific material or carrier type. In such devices, the technique should rather be used as qualitative assessment of charge carrier dynamics, e.g., to analyze differences between devices or to identify systematic changes upon degradation.

C. Simulation methods

Because for state-of-the-art multilayer OLED stacks, the above presented analytical formulas are only of limited validity to determine material parameters, full device modeling should be used preferably. The electrical simulations applied in the present study are based on the drift-diffusion approach that has been presented in many previous publications.^{17,31,38} The equations can be solved

in steady-state, transient and frequency domain to reproduce the measured curves of the electrical experiments, as described in Sec. II B. For electro-optical simulations, the calculated exciton densities are transferred to the optical solver that is based on the dipole emission and transfer matrix models.^{57,58} The commercially available simulation software Setfos is used in this study.⁵⁹

The required inputs for the simulation are the layer sequence with respective thicknesses, the refractive indices, and the electrical and excitonic material parameters (see Table I) of each layer. Here,

for simplification, and motivated by the band diagram in Fig. 1(a), we choose discrete energy levels for transport and traps. For the emitter layer, charge transport is assumed to occur on the mCBP HOMO (holes) and the LUMO of the emitter (electrons). In this example, the OLED stack consists mostly of standard materials without any electrical doping. Many of these materials have been characterized in previous studies that allow us to model directly the full OLED using starting parameters from the literature. For more complicated device structures, it is recommended to start with

TABLE I. Input and fit parameters for opto-electrical simulations.

Parameter	Initial parameter (Fig. 4)	First fit (Fig. 6)	Best fit (Fig. 8)
Series resistance, $R_s^{a,b}$ (Ω)	31–36	31–36	31–36
Parallel resistance, $R_p^{a,b}$ ($M\Omega$)	6.7	6.7	6.7
Hole injection barrier/work function ITO (eV)	0.41/5.0	0.459/4.951	0.37/5.04
Electron injection barrier/work function LiQ/Al (eV)	0.3/3.2	0.335/3.085	0.335/3.085
NPB HOMO/LUMO level (eV)	5.41/2.23	5.41/2.08	5.41/2.08
NPB density of chargeable sites, N_0^c (m^{-3})	10^{27}	10^{27}	10^{27}
NPB relative permittivity, ϵ^a	2.795	2.795	2.795
NPB zero-field hole mobility, $\mu_{p,0}$ ($cm^2 V^{-1} s^{-1}$)	1.0×10^{-4} (Ref. 68)	1.14×10^{-4}	8.69×10^{-5}
NPB field-enhancement coefficient for holes, γ_p ($m^{1/2} V^{-1/2}$)	4.0×10^{-4} (Ref. 68)	1.13×10^{-3}	1.0×10^{-3}
NPB hole trap density, p_t (m^{-3})	1.8×10^{24}
NPB hole trap depth, $\Delta E_{t,p}$ (eV)	0.2
NPB hole traps – capture rate ($cm^3 s^{-1}$)	10^{-17}
TCTA HOMO/LUMO level (eV)	5.62/2.15	5.62/2	5.62/2
TCTA density of chargeable sites, N_0^c (m^{-3})	10^{27}	10^{27}	10^{27}
TCTA relative permittivity, ϵ^a	3.035	3.035	3.035
TCTA zero-field hole mobility, $\mu_{p,0}$ ($cm^2 V^{-1} s^{-1}$)	1.4×10^{-4} (Ref. 69)	1.4×10^{-4}	1.4×10^{-4}
TCTA field-enhancement coefficient for holes, γ_p ($m^{1/2} V^{-1/2}$)	10^{-6}	10^{-6}	10^{-6}
TCTA hole trap density, p_t (m^{-3})	5.5×10^{23}
TCTA hole trap depth, $\Delta E_{t,p}$ (eV)	0.35
TCTA hole traps – capture rate ($cm^3 s^{-1}$)	10^{-14}
EML HOMO/LUMO level (eV)	6.02/3.17	6.02/3.02	6.02/3.02
EML density of chargeable sites, N_0^c (m^{-3})	4×10^{26}	4×10^{26}	4×10^{26}
EML relative permittivity, ϵ^a	3.142	3.142	3.142
EML zero-field hole mobility, $\mu_{p,0}$ ($cm^2 V^{-1} s^{-1}$)	3.0×10^{-5} (Ref. 70)	5.95×10^{-5}	1.0×10^{-4}
EML field-enhancement coefficient for holes, γ_p ($m^{1/2} V^{-1/2}$)	7.3×10^{-4}	8.06×10^{-4}	8.06×10^{-4}
EML zero-field electron mobility, $\mu_{n,0}$ ($cm^2 V^{-1} s^{-1}$)	10^{-8}	3.88×10^{-11}	3.88×10^{-11}
EML field-enhancement coefficient for electrons, γ_n ($m^{1/2} V^{-1/2}$)	10^{-6}	10^{-6}	10^{-6}
EML singlet radiative decay rate, $k_{rad,S}$ (s^{-1})	1.73×10^7	1.73×10^7	1.30×10^7
EML triplet non-radiative decay rate, $k_{nr,T}$ (s^{-1})	5.62×10^3	5.62×10^3	7.75×10^3
EML intersystem crossing rate, k_{isc} (s^{-1})	4.77×10^7	4.77×10^7	3.51×10^7
EML reverse intersystem crossing rate, k_{risc} (s^{-1})	6.41×10^5	6.41×10^5	7.83×10^5
NBPhen HOMO/LUMO level (eV)	6.23/2.90	6.23/2.75	6.23/2.75
NBPhen density of chargeable sites, N_0^c (m^{-3})	10^{27}	10^{27}	10^{27}
NBPhen relative permittivity, ϵ^a	2.878	2.878	2.878
NBPhen zero-field electron mobility, $\mu_{n,0}$ ($cm^2 V^{-1} s^{-1}$)	4.2×10^{-4} (Ref. 71)	7.0×10^{-4}	1.0×10^{-4}
NBPhen field-enhancement coefficient for electrons, γ_n ($m^{1/2} V^{-1/2}$)	10^{-6}	10^{-6}	3.0×10^{-4}
NBPhen electron trap density, n_t (m^{-3})	5×10^{23}
NBPhen electron trap depth, $\Delta E_{t,n}$ (eV)	0.308
NBPhen electron traps – capture rate ($cm^3 s^{-1}$)	10^{-20}

^aExtracted from post-processing techniques and fixed during simulation.

^bSlightly different for every device (not a global parameter).

^cEstimated value and fixed for optimization.

simpler, single-carrier devices to determine and establish the material parameters of the involved layers with reduced ambiguity.^{15,19}

D. Protocol

In order to visualize the proposed workflow for the simulation of experimental data to determine device and material parameters, we set up a protocol that is shown as a flow chart in Fig. 2(a). In the next part, this procedure shall be employed to simulate the measured data on the OLED devices presented in Fig. 1. The individual steps of the protocol for the specific research example are described in Fig. 2(b).

A full electrical characterization of an OLED typically consists of various steady-state, transient, and impedance measurements. As a first step, a selection of relevant results has to be performed. In general, it is recommended to consider as many experimental techniques as possible. However, simulating and evaluating more measurements also takes more time. One should, thus, try to select measurements that yield complementary data but avoid to include multiple similar experiments that contain the same information. For instance, injection-CELIV data at one or two different offset voltages are usually enough. In a second step, we determine those device and material parameters that can be extracted from simple post-processing techniques (e.g., series resistance). Next, the initial guess simulation is set up using measured, assumed, or literature values for the missing material parameters. Importantly, in order to minimize the number of free parameters, and in agreement with Occam's razor, the initial model should be as simple as possible. Applied to the present case study, this means, for example, that we shall neglect any trap states at first and only introduce them in case

the simple model fails to properly describe the measured data. After a first simulation of the initial situation, one should vary all fitting parameters to learn about their effect on different measurement techniques. This also allows to manually optimize these parameters in a next step in order to match the experimental data as well as possible. If the agreement after the optimization is not sufficient, new model parameters should be introduced, for example, trap states, and the optimization should be done again. Finally, once the agreement between simulation and measurements is satisfying, the fit quality should be analyzed. This task consists of a parameter correlation^{17,18} and sensitivity^{19,60} analysis.

III. SPECIFIC EXAMPLE

In this section, we will guide the reader through the workflow illustrated in Fig. 2 on the basis of real measurements on OLEDs described in Sec. II A. The selected experimental data that we want to reproduce with device simulations are shown in Fig. 3. For better visibility, we only show the devices with the 40 nm NPB layer in (a) and (e). It should be noted that the approach presented in the following can directly be extended to temperature-dependent measurements. Such an analysis can be beneficial to disentangle different temperature activated processes, such as mobility and charge injection.³⁰ Clearly, adding temperature-dependent data is more demanding both experimentally as well as from a simulation point of view.

A. Selected measurements

The IV curve shows an onset at about 2.2 V for all devices with 40 nm thick NPB. Not shown in Fig. 3(a) are the curves for

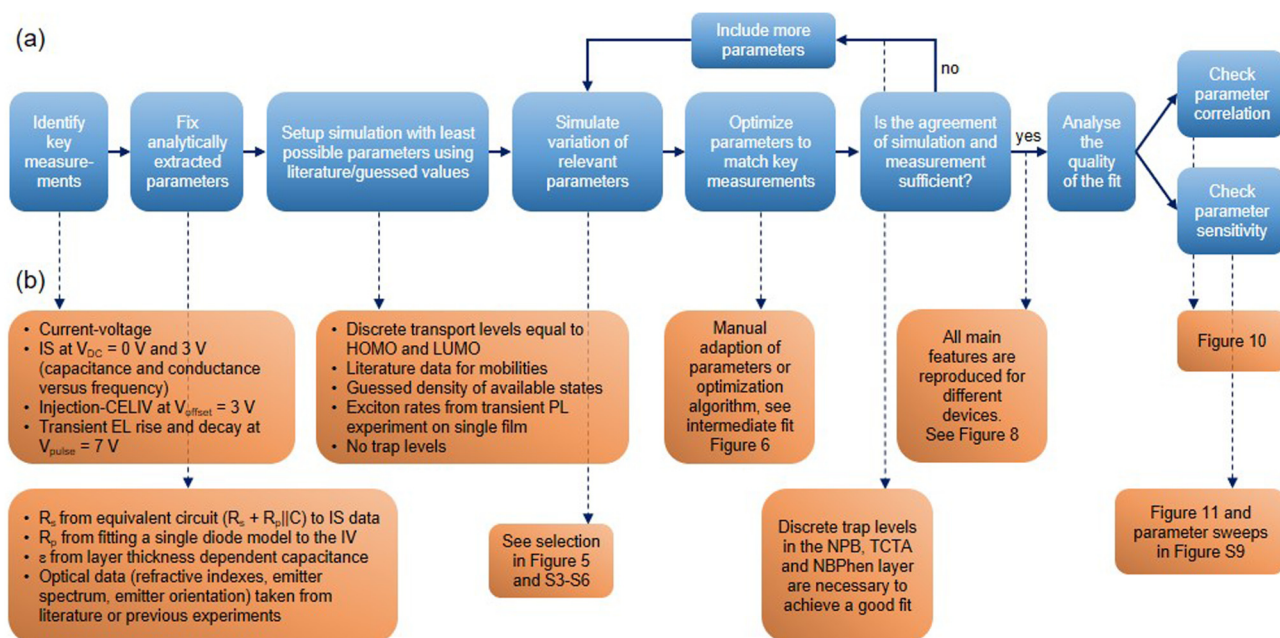


FIG. 2. (a) Workflow to obtain a global fit for various measurement techniques and to analyze the quality of the resulting fit. (b) Example of specific steps in this work.

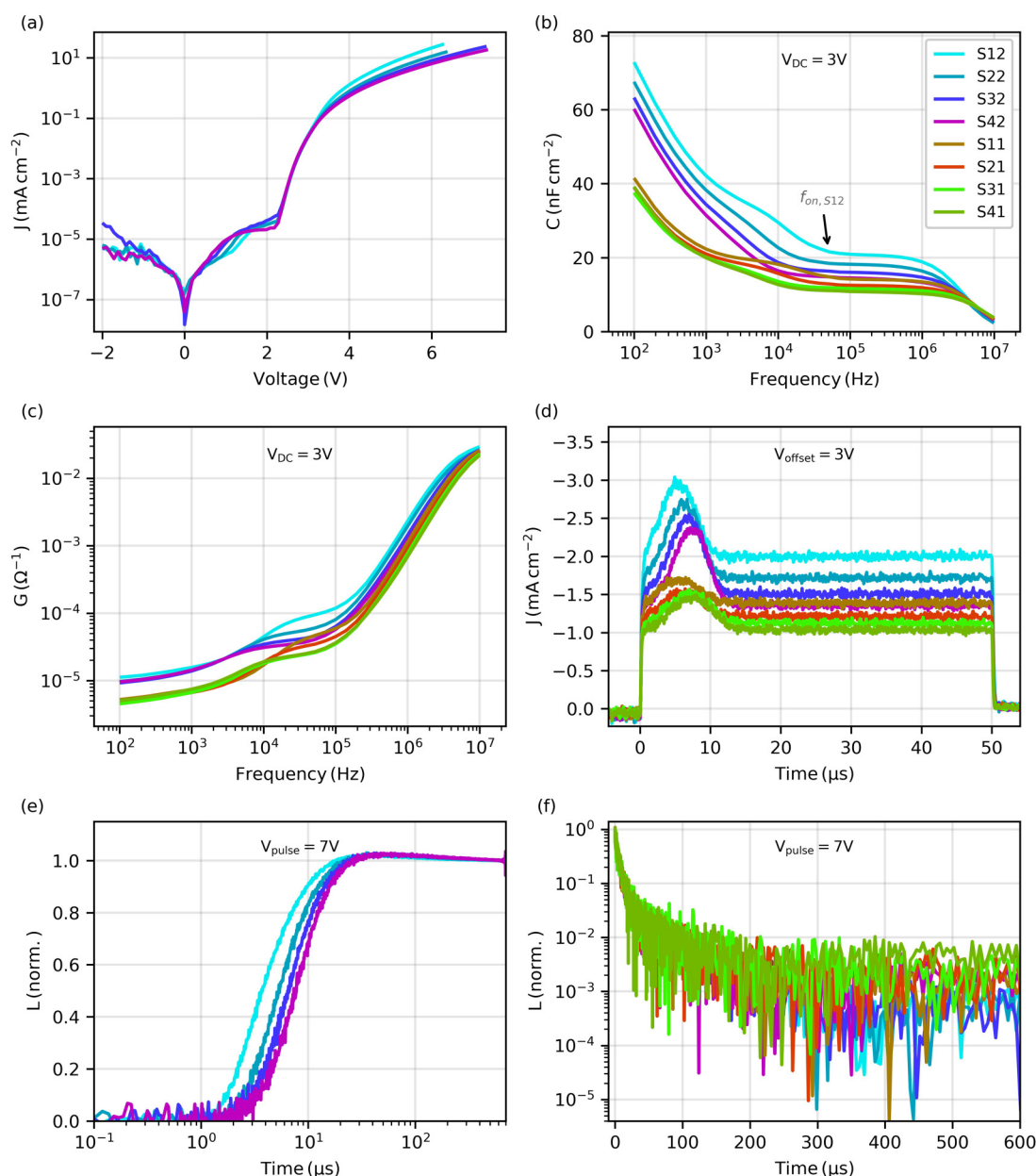


FIG. 3. Selected experimental datasets that will serve as a target in the fitting process. (a) Current–voltage, (b) capacitance–frequency at $V_{DC} = 3\text{ V}$, (c) conductance–frequency at $V_{DC} = 3\text{ V}$, (d) injection-CELIV at $V_{offset} = 3\text{ V}$, transient electroluminescence rise (e), and decay (f) for a voltage pulse of 7 V . In (a) and (e), not all measured eight devices are shown for the sake of visibility (see in Fig. S1 in the [supplementary material](#) for complete data).

the 100 nm thick NPB, which have a slightly higher onset voltage of 2.4 V (see Fig. S1 in the [supplementary material](#)). As this parameter is mostly determined by the built-in potential, it could be speculated that the effect is caused by the fabrication process. Further devices and measurements would be necessary to confirm this hypothesis that goes beyond the scope of this tutorial.

Furthermore, the current in the on state (above 3 V) is systematically reduced with increasing NPB thickness. This indicates that the current at high voltages is limited by hole transport inside the NPB layer.

The capacitance and conductance at $V_{DC} = 3\text{ V}$ are shown in Figs. 3(b) and 3(c), respectively. In the frequency range between

10^5 and 10^6 Hz, the capacitance reflects the geometrical capacitance of the full device, which is also determined at $V_{DC} = 0$ V. Toward lower frequencies, a capacitance rise is observed, which is related to injection of charge carriers. This characteristic frequency f_{on} [see Fig. 3(b)] is independent of the NBPhen layer thickness but shows a dependence on NPB thickness, indicating that the onset is related to hole injection and transport. A second rise is observed at a frequency around 1 kHz for all devices and needs to be linked to a process with slower dynamics.

The conductance between 10^4 and 10^5 Hz shows a similar thickness dependence as IV characteristics at higher voltages. Toward lower frequencies, it converges to one conductance value for all devices that have the same NBPhen thickness, which is in agreement with the current in the IV measurement at the same voltage (3 V). We attribute this behavior to charge carriers (holes) that are already present in the device at 3 V and accumulate either at the TCTA/EML or at the EML/NBPhen interface. The remaining NBPhen (and EML) layer(s) is (are), thus, limiting the conductivity at this voltage.

Injection-CELIV was performed at several offset voltages. For discussion and simulation purposes, we chose an offset voltage of 3 V that is just above the turn-on voltage of the OLED. At this low offset voltage, only small amounts of charges are injected that accumulate at some internal interface and are then extracted by the reverse voltage ramp. As outlined in Sec. II, the peak time is related to the charge carrier mobility. For devices with the same NPB but different NBPhen thickness, the peak occurs at the same time [Fig. 3(b)]. Only the peak area changes, which can be explained by the different amount of charge that was injected. The NPB thickness variation results in a clear peak shift. Judging from the observed independence of t_{max} from the electron transport layer thickness, we can already attribute the peak to an effective hole transport time. However, without knowing the interface at which charges accumulate prior to the CELIV ramp, we cannot estimate a reliable value for the hole mobility. Additionally, for multilayer structures, one can only obtain an average hole mobility that is not directly related to one specific layer. It is worth noting that the measured displacement current plateau value for times $t > 15 \mu s$ is in perfect agreement with the geometric capacitance of the devices measured by impedance spectroscopy.

The TEL rise and decay for a voltage pulse of 7 V are shown in Figs. 3(e) and 3(f), respectively. As discussed in Sec. II B 3, the TEL turn-on time is related to charge transport and injection and shows a similar NPB thickness dependence as the IV curve, the first C - f onset, and the injection-CELIV peak time. As for the injection-CELIV peak, we cannot directly extract mobility using the analytical formula. However, from the thickness trend, we can see that the TEL onset is limited by hole transport to the emission zone. This qualitative understanding can already provide first insight in view of OLED device design and optimization. In addition to the onset time trends, a small luminance overshoot is observed for all devices before they reach their steady-state luminance at the end of the pulse. Below, we will illustrate that this behavior can be related to a trapping effect in one of the hole transport layers.

In the TEL decay, we do not see any difference among the devices of varying thicknesses. By fitting a single exponential decay

to the first decay, we can extract a radiative lifetime of about $5 \mu s$. This agrees well with the delayed fluorescence lifetime of the investigated TADF emitter measured by transient photoluminescence (PL) of the pure emitter film (data not shown). Interestingly, the modified cavity defined by different layer thicknesses does not influence this decay lifetime. This finding might be related to the TADF emitter for which the reverse intersystem crossing is dominating the decay dynamics.

The above qualitative discussion demonstrates how much more information can be obtained for a specific OLED stack if consistent data with varied layer thickness are available. When fitting the experimental data in the following, the value of the complementary data set becomes even more evident.

B. Setting up the simulation

As indicated in Fig. 2(a), some device and material parameters can directly be extracted from the measurements and should be determined before setting up the simulation. The first parameters are the external series resistance R_s and parallel resistance R_p of the cells. As they depend on the contact quality as well as some shunts that may occur for one or the other cell, these parameters are extracted for each cell and not considered as global parameters. Nevertheless, it turns out that these values are very similar for all the tested devices reported here. R_s is determined by fitting the C - f measurement at $V_{DC} = 0$ V with an equivalent circuit model ($R_s + [R_p || C]$). A single diode model was adapted to the IV curve to give R_p .¹⁷ The resulting values are given in Table I.

Further parameters that can be determined directly from the measurement data are the relative permittivities ϵ of the individual organic layers. First, one has to ensure that the C - f plateau at $V_{DC} = 0$ V corresponds to the geometrical capacitance of all the semiconducting layers. This was checked by multiplying the capacitance with the total thickness. All devices with varied NPB and NBPhen layer thicknesses give almost the same value that indicates that we are probing the full device. Especially, if highly doped or intrinsically polar layers are included, this condition is not necessarily fulfilled and the extraction of the relative permittivity is more difficult.^{19,21} Here, the geometrical capacitance of the total device is determined from the C - f plateau at $V_{DC} = 0$ V. Assuming a parallel plate capacitor for each layer, the total capacitance is given by a serial connection of each layer's capacitance. Thanks to the variation of the NPB (NBPhen) thickness, we can directly plot C^{-1} vs d_{NPB} (d_{NBPhen}) (see Fig. S2 in the supplementary material), which is supposed to be linear with a slope corresponding to the permittivity of NPB (NBPhen). The permittivity of TCTA and the EML cannot be independently extracted as there is no thickness variation of these layers. The analytically extracted parameters are marked by footnote "a" in Table I and are kept fixed during the following simulations.

In order to perform a full electro-optical simulation, we also need refractive indices of all the layers. Most of them are available from the Setfos database or were taken from the literature.^{59,61,62} For the EML, spectroscopic ellipsometry was performed on a film. Furthermore, the emitter source spectrum was measured by PL on a pure emitter film. The HOMO and LUMO energies were taken from the literature.^{16,20,22,63–65} Due to the uncertainty in the

determination of the LUMO,^{66,67} this parameter was allowed to be changed by up to 0.5 eV during the fitting. The remaining electrical parameters, i.e., hole and electron injection barriers, density of chargeable sites, and hole and electron mobilities for each of the layers, were guessed or taken from the literature if available.^{68–71} Here, the respective mobilities are described by the field-dependent

Poole–Frenkel mobility model,

$$\mu(E) = \mu_0 e^{\gamma\sqrt{|E|}}, \quad (4)$$

where μ_0 is the zero-field mobility, γ is the field-enhancement factor, and E is the electric field. By the choice of this mobility

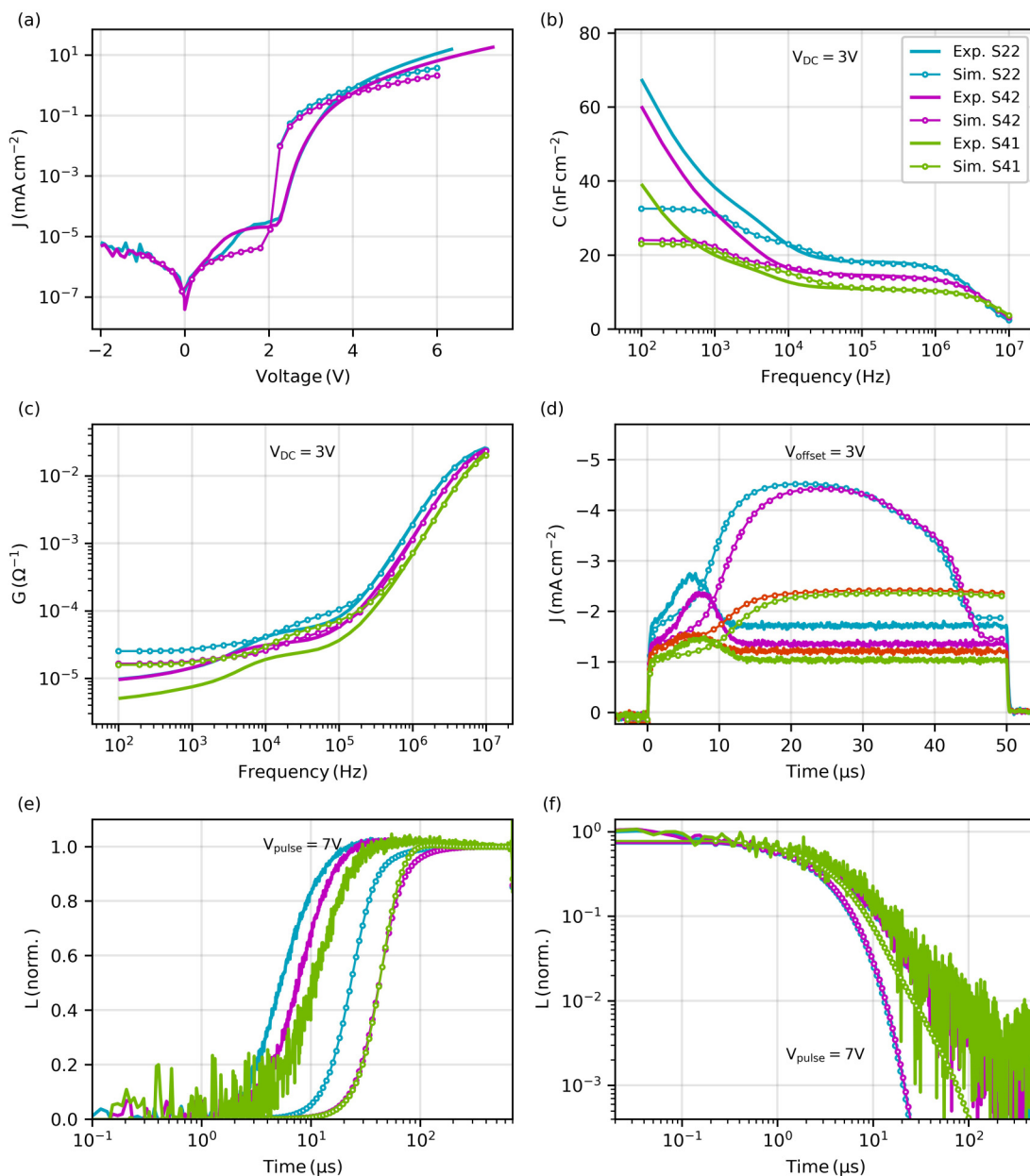


FIG. 4. Measured data (solid line) and simulation using the initial parameter set shown in Table I: (a) Current–voltage, (b) capacitance–frequency at $V_{DC} = 3$ V, (c) conductance–frequency at $V_{DC} = 3$ V, (d) injection-CELIV at $V_{offset} = 3$ V, transient electroluminescence rise (e), and decay (f) for a voltage pulse of 7 V. For better visibility, only selected devices are shown.

model, with only two free parameters, we follow the principle of Occam's razor, which states that the least complex model that can explain all observations should always be preferred. This parametrization of charge mobility does not include any direct charge carrier dependence. If temperature-dependent measurements were included, both charge- and field-dependence could be considered more easily by employing the extended Gaussian/correlated disorder model (EGDM/ECDM).^{72,73} While the solution of the EGDM/ECDM has been presented before in steady-state, the implementation to solve multilayer structures in time and frequency domain is much more involved. As the inclusion of transient and impedance data plays a key role in this analysis, we choose the Poole-Frenkel mobility model that is the simplest model at room temperature that can well describe the presented experimental data.

Whenever more complicated device structures, doped layers, or new transport materials are investigated, it is generally useful to first measure and simulate elementary devices, such as single-carrier devices, and then gradually increase the complexity of the investigated stack.¹⁵ It has to be noted here that the choice for the mobility values of the minority carriers, i.e., the electron (hole) mobilities in the NPB and TCTA (NBPhen), has a negligible effect

on the simulated curves. Therefore, they are not used as fitting parameters in the following and not mentioned in Table I. To couple the electrical characteristics with the optical measurements, excitonic parameters have to be known. For our TADF system, radiative, non-radiative, and intersystem crossing rates were extracted from a transient PL experiment with an emitter film sample. These parameters were used as input for the initial guess simulation. All initial electronic and excitonic parameters are given in Table I.

For the first simulations (initial guess), the assumed model is as simple as possible, i.e., no trap states are included in any of the layers. Starting from this model using the above initial parameters, we can now perform the simulations for each of the measurement techniques and device configurations (see Fig. 4).

The initial forward simulation is well capable of reproducing some trends, e.g., the HTL thickness dependence in the IV . Nevertheless, several important experimental observations are not yet well captured by the simulations. An obvious example is the TEL rise that occurs about one order of magnitude too late in the simulation compared to the experiment. Thanks to the trends with varied NPB and NBPhen layer thickness, we can already conclude that we need to adjust the hole mobility in one of the hole

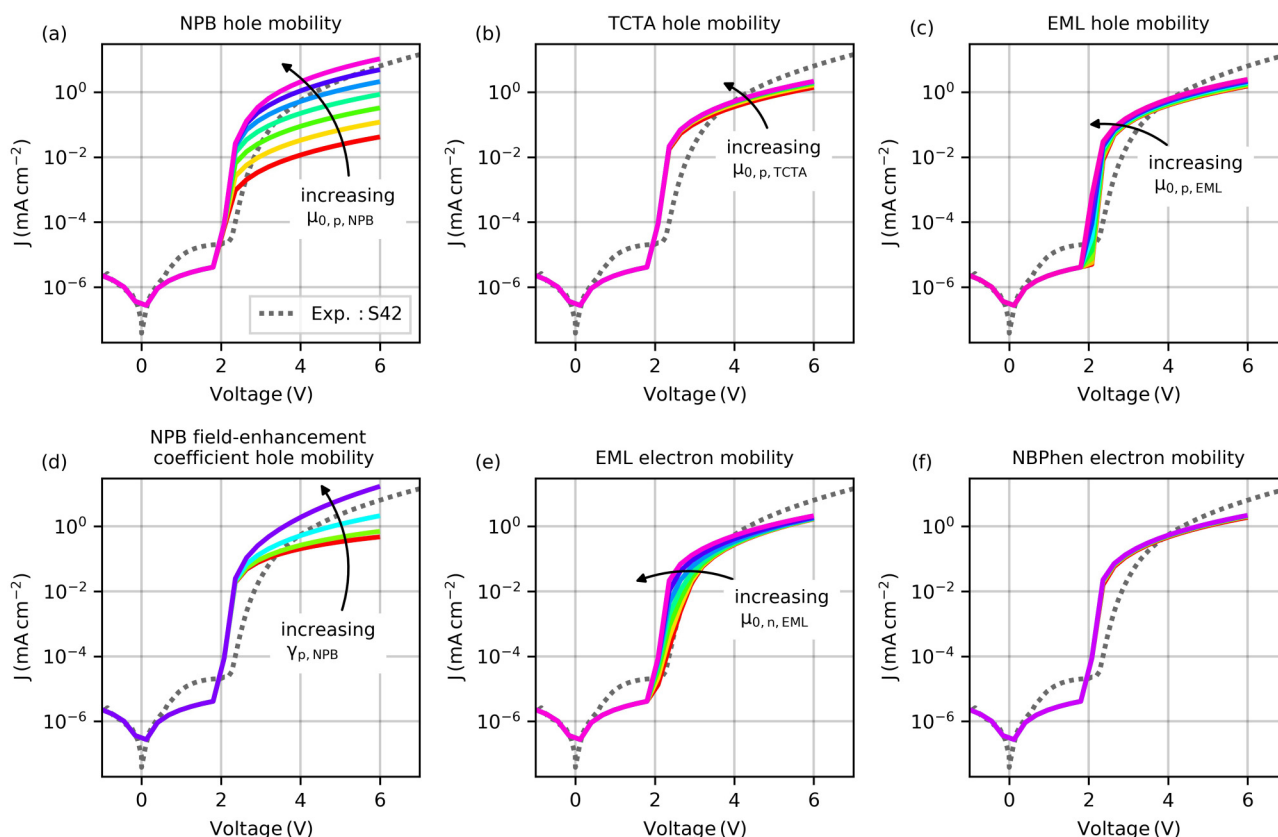


FIG. 5. Influence of the material parameters: (a) NPB, (b) TCTA, (c) EML zero-field hole mobility, (d) NPB mobility field-enhancement factor, (e) EML, and (f) NBPhen zero-field electron mobility on the simulated IV curve. The dashed gray line represents the measurement on device S42.

transport layers or the EML, or the hole (injection) barriers between the layers.

In Sec. III C, we will systematically assess the influence of the parameters on the simulated curves and adapt them to obtain a quantitative agreement with the measured characteristics.

C. Fitting the experimental results

First, we notice that the simulated IV onset voltage (V_{onset}) is not in agreement with the measurements. The only parameter that influences this voltage is the built-in potential. In order to match the measured onset, we, therefore, decrease all LUMO levels by

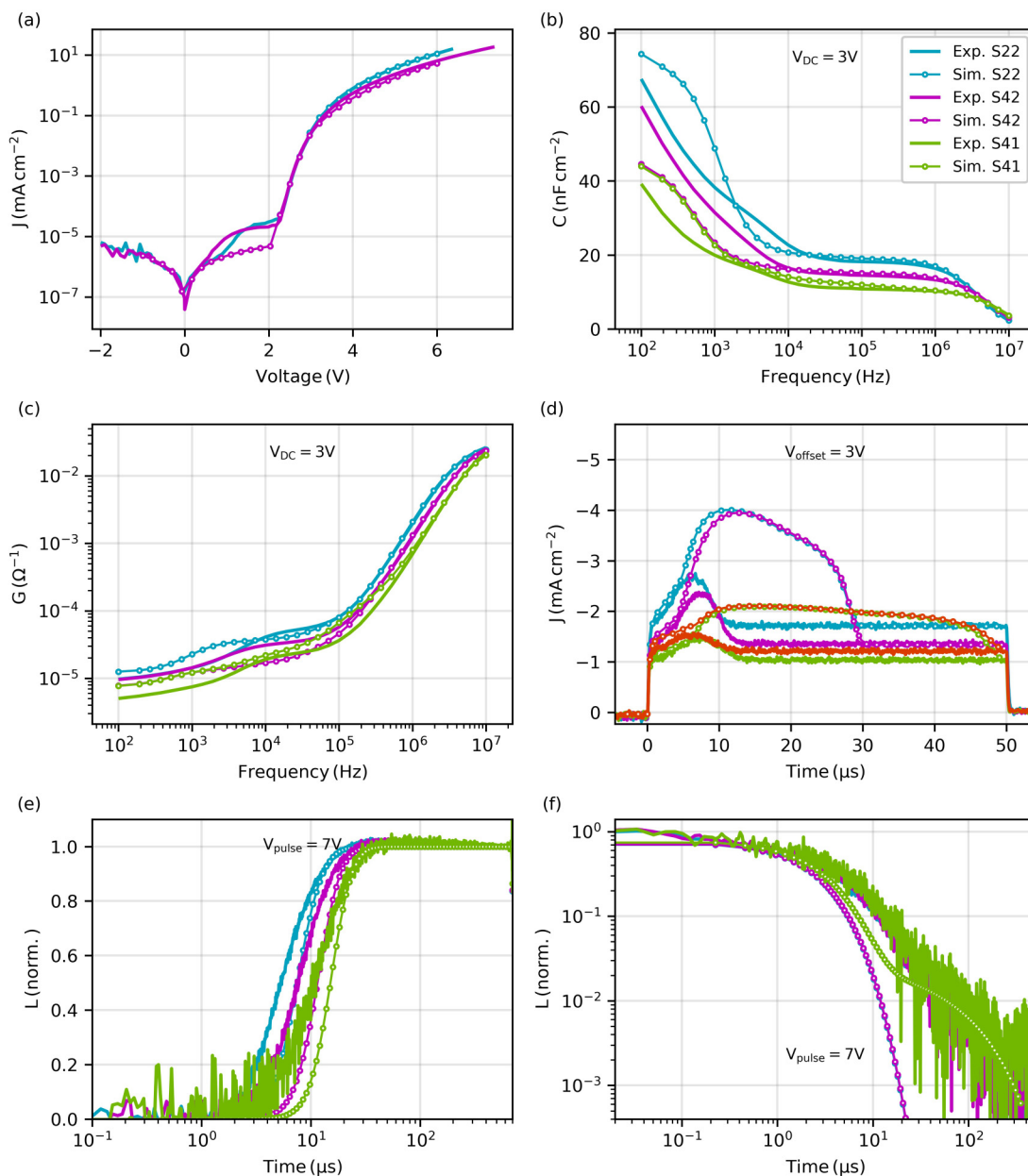


FIG. 6. First fit of the selected measurements without considering any trap states. The simulations are shown as solid lines with open circles. The parameters for the simulation are listed in Table I. (a) Current–voltage, (b) capacitance–frequency at $V_{\text{DC}} = 3\text{ V}$, (c) conductance–frequency at $V_{\text{DC}} = 3\text{ V}$, (d) injection-CELIV at $V_{\text{offset}} = 3\text{ V}$, transient electroluminescence rise (e), and decay (f) for a voltage pulse of 7 V. For better visibility, only selected devices are shown.

0.15 eV in energy while keeping the energy barriers the same. After this adaption, the energy levels are now fixed for all the following optimization steps.

As mentioned above, thanks to the thickness dependence we already know that some hole mobilities have to be increased in the simulation to improve the agreement with the measurement in TEL rise and injection-CELIV. However, we cannot easily distinguish between the hole mobility in NPB, TCTA, or in the EML. In order to quantitatively understand which parameter is influencing the electrical device characteristics in which way, we perform individual parameter sweeps starting from the initial simulation shown in Fig. 4. As examples, we show the influence of the NPB, TCTA, EML zero-field hole mobilities, the field-enhancement coefficient for NPB as well as the zero-field electron mobilities in the EML and the NBPhen on the *IV* (Fig. 5), the TEL rise, the injection-CELIV signal, and the *C-f* plot (Figs. S4–S6 in the [supplementary material](#)). In order to simplify the graph, we only show the parameter variation for device S42.

The largest influence on the *IV* curve is observed for the zero-field hole mobility and the field-enhancement factor of the NPB. While the former gradually increases the forward current, the latter also influences the power law of the current above 2.5 V.

Thus, we will clearly need to increase the latter in order to fit the experimental data. Interestingly, the charge carrier mobilities in the EML mostly affect the region just after V_{onset} . Especially, the electron mobility should be decreased to match the slope of *IV* between 2 and 3 V. The TCTA hole mobility and the NBPhen electron mobility have only a minor effect on the simulated *IV* curve. Using only these six parameters would allow to obtain a decent fit of the *IV* curve. However, we also want to include the impedance and transient signals in order to increase the reliability of the extracted parameters. This is illustrated by the cases of the hole and electron mobilities in the EML, which affect *IV* only slightly. While the EML hole mobility clearly shifts the TEL onset, the electron mobility has no effect on the onset time (Fig. S6 in the [supplementary material](#)). In the case of injection-CELIV, both mobilities have an influence on the peak position t_{max} : increasing or decreasing the EML hole or electron mobility shifts the peak position to shorter or longer times, respectively. This example highlights the importance of combining several measurement techniques, as the unknown parameters are reflected differently in each experiment.

As a next step, we will adjust the parameters to match the simulation with the selected key measurements. This can either

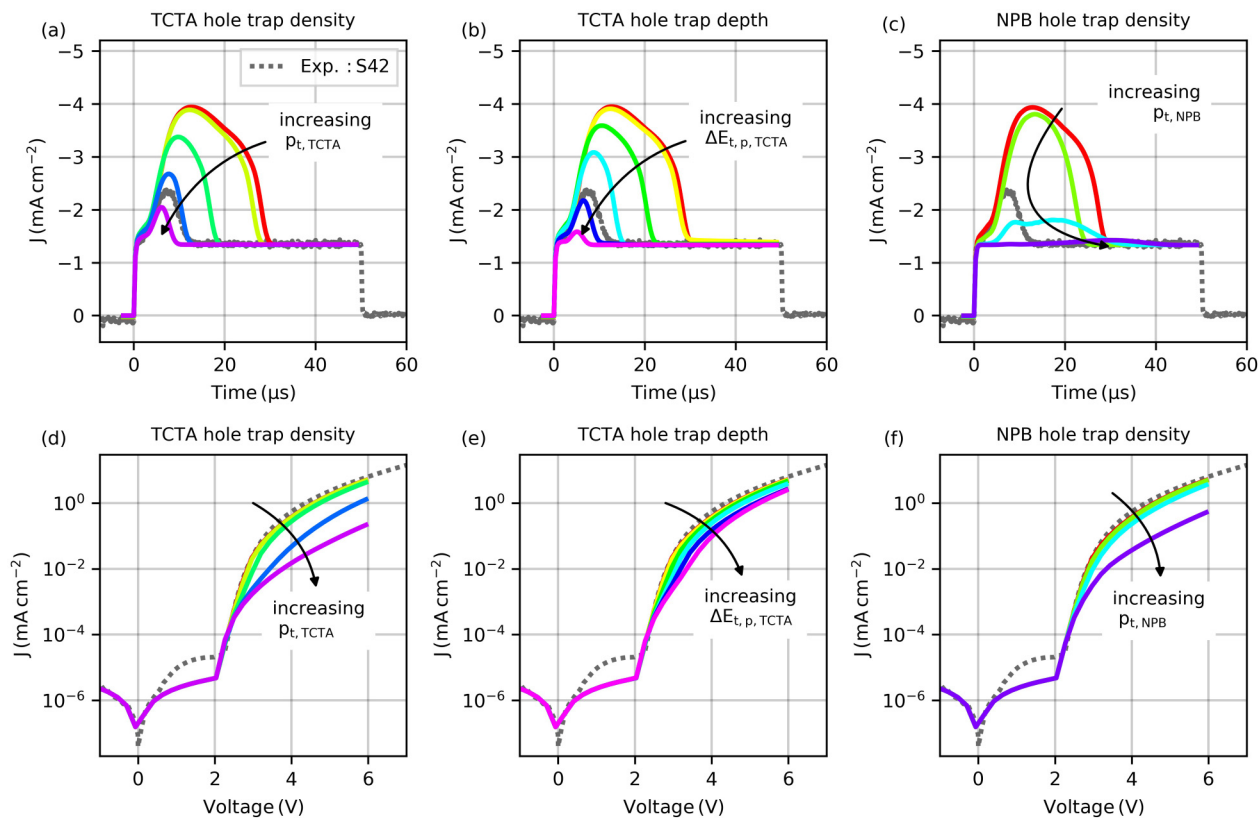


FIG. 7. Influence of the trap parameters in TCTA (a), (b), (d), (e) and NPB layer (c), (f) on the simulated injection-CELIV (a)–(c) and *IV* curve (d)–(f). The dashed gray line represents the measurement on device S42.

be done with an automatic optimization/fitting algorithm or by manual tweaking of single parameters according to the observations in the parameter sweeps (Fig. 5 and Figs. S4–S6 in the supplementary material). Automatic least-square fitting algorithms, such as Levenberg–Marquardt or simulated annealing, try to minimize the error χ between the measurement m and the simulation s for N user-defined target points that can be

weighted by a factor w ,

$$\chi^2 = \sum_{i=1}^N f_i^2 = \sum_{i=1}^N (w_i(m_i - s_i))^2. \quad (5)$$

Due to multiple devices and measurement techniques that should be optimized together, the selection of the target points and

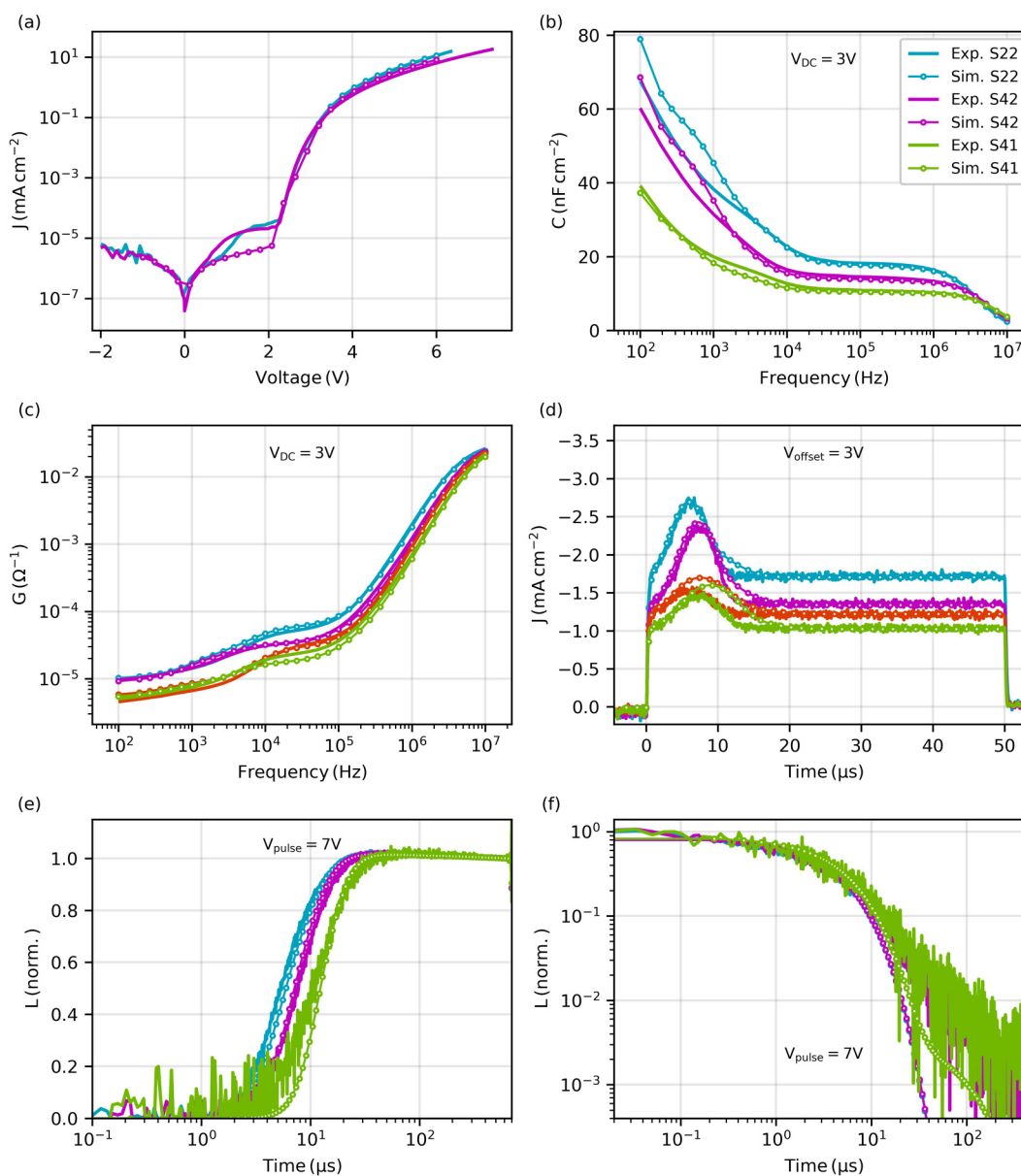


FIG. 8. Final fit of the selected measurements considering traps in NPB, TCTA, and NBPhen layers. The simulations are shown as solid line with open circles. The parameters for the simulation are listed in Table 1. (a) Current–voltage, (b) capacitance–frequency at $V_{DC} = 3$ V, (c) conductance–frequency at $V_{DC} = 3$ V, (d) injection-CELIV at $V_{offset} = 3$ V, transient electroluminescence rise (e), and decay (f) for a voltage pulse of 7 V. For better visibility, only selected devices are shown.

individual weighting factors w_i is not straightforward. The optimization is, therefore, done manually in this example. Furthermore, the fit quality is not evaluated quantitatively by an absolute error but judged by eye. The best fit that was obtained for the current model (no traps included) is shown in Fig. 6.

This first fit is already able to reproduce the IV curve above turn-on very well. Also, the trends with varied NPB and NBPhen layer thicknesses in the TEL and injection-CELIV curves are well reproduced. However, the injection-CELIV peak is clearly too large, which indicates that too many charge carriers are accumulated and extracted in the modeled device. The simulated impedance data show quantitatively the same result as the measured $C-f$ and $G-f$ characteristics at 3 V. The NBPhen thickness dependence is, however, not correctly reproduced. Finally, also the fit of TEL decay [Fig. 6(f)] still needs some fine tuning of the parameters. This measurement is the only one that is dominated by excitonic parameters, i.e., $k_{\text{rad},S}$, $k_{\text{nr},T}$, $k_{\text{isc},C}$, and $k_{\text{risc},C}$. These parameters can, therefore, be independently adapted to match the TEL decay signal. The modifications are listed in Table I, and the resulting simulated TEL decay curve is shown in Fig. 8(f).

The other electro-optical simulations cannot be adapted further to improve the agreement with the experimental data using the existing model that does not consider any trap states. Therefore, according to the workflow in Fig. 2, we shall diversify the model and include additional material parameters. The main features that we want to reproduce in a better way with the simulations are (1) the injection-CELIV peak area that is currently too large in the simulation, as well as (2) the NBPhen thickness dependence in the $C-f$ and $G-f$ data. As mentioned before, the injection-CELIV transient at $V_{\text{offset}} = 3$ V is mainly determined by hole transport parameters. We, therefore, first analyze the effect of including hole traps in the NPB, TCTA, and the EML. We find that including hole traps in the EML does not affect the injection-CELIV peak at all. Therefore, we do not further consider any hole traps in this layer. In striking contrast, for the NPB and TCTA layers, the hole trap density as well as the trap energy in TCTA have a significant impact on the CELIV peak area. The corresponding simulations of the injection-CELIV and the IV curve are shown in Fig. 7. In more detail, we see that both the TCTA hole trap density and the trap depth have a very similar influence on the CELIV transient and to some extent also on the IV curve. This indicates that the parameters “trap density p_t ” and “trap depth $\Delta E_{t,p}$ ” are correlated, which will also be discussed and quantified in Sec. III D. Furthermore, we see from Fig. 7 that including as many TCTA traps as necessary to match the injection-CELIV peak area will clearly deteriorate the IV behavior. We will, therefore, also need to include some traps in the NPB layer.

The effect of the NPB trap density is shown in Figs. 7(c) and 7(f). As for the TCTA layer, the traps’ depth has a very similar effect on the simulated curves as their density (see Fig. S7 in the supplementary material). In contrast to the traps in the TCTA layer, which mainly shift the CELIV peak in time while the qualitative shape is maintained, the traps in the NPB also change the shape of the injection-CELIV peak. In some cases, even a double peak is observed. In order to find a good fit for both the IV and the injection-CELIV data, we need to include and optimize the trap parameters in both NPB and the TCTA layers. As an additional positive effect, the inclusion of hole traps in TCTA and NPB leads

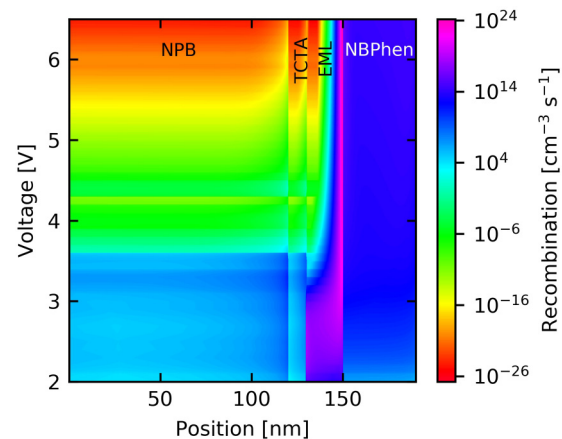


FIG. 9. Steady-state recombination profile as a function of the applied voltage.

to a small TEL overshoot in the simulation, which was also confirmed experimentally. Without trap states, the simulated TEL signal never exhibits an overshoot. The overshoot height can be adjusted by the capture rate of hole traps in TCTA and NPB layers.

In order to reproduce the measured NBPhen thickness dependence in the IS data, it is required to introduce electron traps in this layer. As shown in Figs. 6(b) and 6(c), the simulated capacitance and conductance of samples S41 and S42 converge to the same low frequency value, while a clear thickness dependence is observed in the measurement. Gradually increasing the trap density or the trap depth will increase the distance between the simulated curves of devices S41 and S42. Again, this demonstrates the importance of having several devices with varied layer thicknesses. It would not have been possible to identify the presence of trap states in the NBPhen if there would have been only devices with one layer thickness.

After optimizing the trap parameters together with the other electronic material parameters, we obtain the final fit shown in Fig. 8. We can see that all the main features in the measurements are well captured for all the devices. Remarkably, the global fit covers eight devices with different NPB and NBPhen layer thickness combinations using a single same set of material parameters.

Before the reliability of the extracted material parameters is analyzed in Sec. III D, we show how the simulation can further be used to understand device performance and analyze possible loss mechanisms. First, it is possible to analyze electrical profiles of the device at any working point. As an example, Fig. 9 shows the recombination profile of the S42 device as a function of voltage. The recombination between 2 and 3 V is almost constant in the full EML. With higher voltages, the recombination zone gets narrower and settles at the EML/NBPhen interface. This is in agreement with previous findings by Peng *et al.*, who reported an exponentially decaying emission zone at the ETL interface with a width of about 7 nm using a very similar OLED structure.²² Such an accumulation of charge carriers at one interface of the EML is not ideal because degradation of organic molecules will predominantly occur at

Final Fit - Correlation Matrix

NPB $\mu_{p,0}$	1.00	0.70	0.07	-0.31	0.02	0.04	-0.15	-0.11	-0.03	-0.08	-0.41	-0.05	-0.15	-0.08	0.29	0.24	0.24	0.14	-0.00	0.01	-0.00
NPB γ_p	0.70	1.00	0.25	0.02	0.04	0.07	-0.10	-0.16	0.15	0.29	-0.49	-0.11	-0.32	-0.19	-0.01	0.29	0.29	0.04	-0.08	-0.04	-0.00
TCTA $\mu_{p,0}$	-0.07	0.25	1.00	0.11	0.27	0.28	-0.19	-0.29	-0.02	0.11	-0.02	-0.01	-0.55	-0.51	-0.10	0.46	0.27	-0.05	0.03	0.02	0.00
TCTA γ_p	-0.31	0.02	0.11	1.00	-0.06	-0.06	0.27	-0.00	0.16	0.38	0.05	0.05	-0.04	-0.01	-0.92	-0.02	0.02	-0.32	0.04	0.04	0.00
EML $\mu_{p,0}$	-0.02	0.04	0.27	-0.06	1.00	0.99	0.28	0.38	0.03	-0.02	0.01	0.01	0.05	0.06	-0.00	-0.18	0.08	-0.31	-0.07	-0.01	0.00
EML γ_p	-0.04	0.07	0.28	-0.06	0.99	1.00	0.21	0.33	-0.02	-0.04	-0.03	0.02	0.04	0.05	-0.00	-0.18	0.10	-0.34	-0.00	0.08	-0.00
EML $\mu_{n,0}$	-0.15	-0.10	-0.19	0.27	0.28	0.21	1.00	0.93	0.21	0.15	0.20	-0.30	0.00	0.01	-0.20	-0.38	-0.38	0.01	-0.29	-0.18	0.02
EML γ_n	-0.11	-0.16	-0.29	-0.00	0.38	0.33	0.93	1.00	0.14	0.03	0.20	-0.23	0.04	0.03	0.04	-0.51	-0.47	0.05	-0.24	-0.13	0.01
NBPhen $\mu_{n,0}$	-0.03	0.15	-0.02	0.16	0.03	-0.02	0.21	0.14	1.00	0.81	-0.14	-0.31	-0.05	-0.05	-0.10	-0.27	-0.28	0.08	-0.84	-0.76	0.00
NBPhen γ_n	-0.08	0.29	0.11	0.38	-0.02	-0.04	0.15	0.03	0.81	1.00	-0.21	-0.31	-0.07	-0.04	-0.31	-0.12	-0.17	0.01	-0.63	-0.58	0.00
Δ_h	-0.41	-0.49	-0.02	0.05	0.01	-0.03	0.20	0.20	-0.14	-0.21	1.00	-0.43	0.11	0.10	-0.04	-0.03	-0.01	-0.06	-0.14	-0.08	-0.01
Δ_e	-0.05	-0.11	-0.01	0.05	0.01	0.02	-0.30	-0.23	-0.31	-0.31	-0.43	1.00	0.03	0.03	-0.12	0.05	0.09	-0.09	0.69	0.54	-0.09
NPB ρ_t	-0.15	-0.32	-0.55	-0.04	0.05	0.04	0.00	0.04	-0.05	-0.07	0.11	0.03	1.00	0.97	0.04	0.20	0.44	0.01	0.00	-0.03	0.01
NPB $\Delta E_{t,p}$	-0.08	-0.19	-0.51	-0.01	0.06	0.05	0.01	0.03	-0.05	-0.04	0.10	0.03	0.97	1.00	-0.01	0.24	0.49	-0.03	0.03	0.03	-0.00
NPB $C_{p,t}$	-0.29	-0.01	-0.10	-0.92	-0.00	-0.00	-0.20	0.04	-0.10	-0.31	-0.04	-0.12	0.04	-0.01	1.00	0.05	-0.06	0.48	-0.10	-0.10	0.33
TCTA ρ_t	-0.24	0.29	0.46	-0.02	-0.18	-0.18	-0.38	-0.51	-0.27	-0.12	-0.03	0.05	0.20	0.24	0.05	1.00	0.86	0.22	0.21	0.14	-0.00
TCTA $\Delta E_{t,p}$	-0.24	0.29	0.27	0.02	0.08	0.10	-0.38	-0.47	-0.28	-0.17	-0.01	0.09	0.44	0.49	-0.06	0.86	1.00	-0.19	0.24	0.21	-0.00
TCTA $C_{p,t}$	-0.14	0.04	-0.05	-0.32	-0.31	-0.34	0.01	0.05	0.08	0.01	-0.06	-0.09	0.01	-0.03	0.48	0.22	-0.19	1.00	-0.13	-0.18	0.00
NBPhen n_t	-0.00	-0.08	0.03	0.04	-0.07	-0.00	-0.29	-0.24	-0.84	-0.63	-0.14	0.69	0.00	0.03	-0.10	0.21	0.24	-0.13	1.00	0.93	-0.04
NBPhen $\Delta E_{t,n}$	-0.01	-0.04	0.02	0.04	-0.01	0.08	-0.18	-0.13	-0.76	-0.58	-0.08	0.54	-0.03	0.03	-0.10	0.14	0.21	-0.18	0.93	1.00	-0.03
NBPhen $C_{n,t}$	-0.00	-0.00	0.00	0.00	0.00	-0.00	0.02	0.01	0.00	0.00	-0.01	-0.09	0.01	-0.00	0.33	-0.00	-0.00	0.00	-0.04	-0.03	1.00

FIG. 10. Correlation matrix of the final fit is shown in Fig. 8. Only the correlations among the parameters that were used to fit the experimental curves are calculated. The measurement techniques that are considered are *IV* between -1 and 6 V, *C-f* and *G-f* at offset voltages 1 , 2 , and 3 V, injection-CELIV at $V=3$ V, as well as TEL rise at 7 V.

locations of high charge carrier and exciton concentrations.^{22,74,75} A broadening of the emission zone is, therefore, desirable to increase the stability of this OLED structure. In this example, the electron transport in the EML host-guest layer is assumed to occur on the emitter molecules themselves. Because the emitter concentration is low (20%), the electron transport is limited, which is also reflected in the extracted mobility parameters for the EML (see Table I). The zero-field electron mobility is about seven orders of magnitude smaller than the zero-field hole mobility of the EML. Balancing the EML mobilities would broaden the recombination zone, which could

improve the lifetime of these devices. Such an electron mobility increase can, for example, be achieved by using a co-host approach or by increasing the emitter concentration.²²

Similarly, one could also look at the charge density profiles during the TEL rise (see Fig. S8 in the supplementary material) to understand, for example, which charge carrier type is limiting the onset time. As expected from the experimental thickness dependence, the electrons can already reach the EML/NPhen interface before the actual TEL onset, while the overall hole density, and thus the recombination, only increases after 2 and $10 \mu\text{s}$. Thanks to the simulation,

we can confirm that the TEL onset time is determined by hole transport in this OLED.

D. Analysis of the fit quality

The last steps after obtaining the global fit shown in Fig. 8 are to analyze the reliability of the extracted device and material parameters listed in Table I. The reliability aspect of the parameters consists of two attributes: the correlation and the sensitivity.

Correlation between parameters A and B basically indicates that changing A has the same effect on the simulated curve (or on the fitting error) as changing B. The linear correlation between two parameters can be quantified mathematically. It is calculated from the derivative of the errors f_i defined in Eq. (5) with respect to the model parameter at all user-defined target points N . The interested reader is referred to Refs. 17 and 18 for more details.

In Fig. 10, the correlations between all fitted material parameters are shown, expressed in values between -1 (fully negatively correlated) and $+1$ (fully positively correlated). A value of 0 means that the parameters are not correlated. The main remaining positive linear correlations (most saturated colors) are observed for the zero-field mobilities with their corresponding field-enhancement coefficients and for the trap densities with the respective trap depth. The latter was already indicated in Sec. III C and can be seen in Fig. 7 (Fig. S7 in the supplementary material) where both TCTA (NPB) trap parameters show the same effect on the injection-CELIV transient and the IV curve. In order to reduce this correlation, it is suggested to add temperature-dependent measurement data to the fit. A few other correlations are also apparent, e.g., for the NBPhen trap density and depth with the NBPhen electron mobility parameters. Overall, the average linear correlation (mean value of all off-diagonal elements in Fig. 10) is 0.18. When only IV curves are included in the correlation analysis, a mean value of 0.68 is obtained. This highlights the importance of combining complementary experiments in the analysis, in order to reduce the parameter correlation. As a general guideline, we suggest to target correlation values below 0.5.

Correlations can increase with the complexity of the model and consequently the number of parameters that we introduce. It should, therefore, be emphasized again that the model should be kept as simple as possible to fit the measured data. This ensures that a high reliability of extracted parameters is maintained.

A second criterion to assess the reliability of the extracted parameters is the sensitivity of the investigated characterization techniques to the material parameters. Parameter sensitivity analysis can be divided into a local and a global one. The first evaluates the influence of a parameter variation around a specific local working point on the agreement between simulation and measurement. Here, the sensitivity is evaluated for the final fitting parameters as working point, yielding the sensitivity of the final fit (Fig. 8) on each of the parameters.

Global sensitivity analyzes the combined effect of varying all parameters within a certain range. These randomized simulation results are typically shown as scatterplots.⁷⁶ While it can give more general insights into the sensitivity of specific measurement techniques to material parameters, it is more difficult to be quantified compared to the local sensitivity analysis and computationally

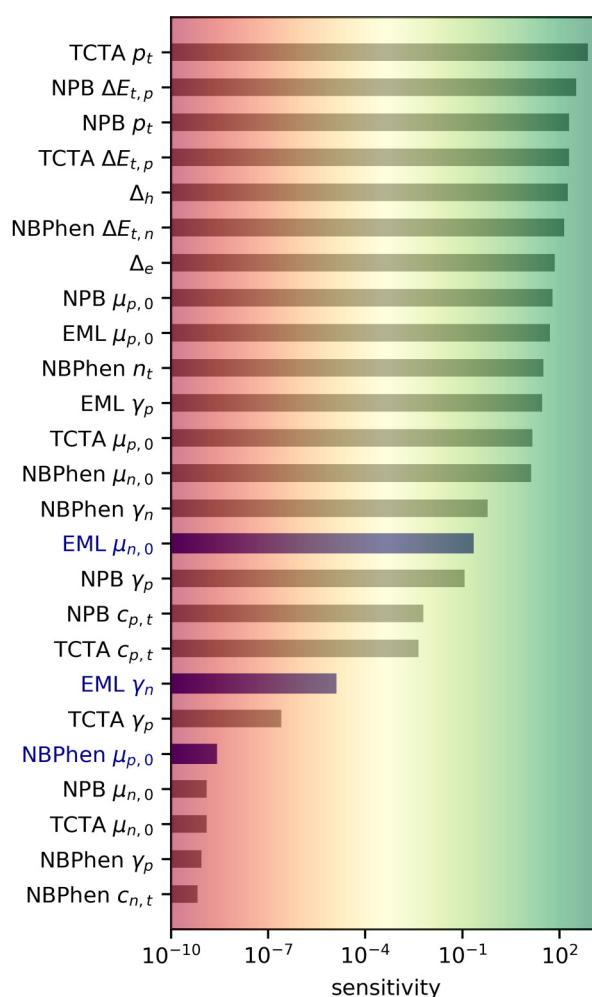


FIG. 11. Local sensitivity of electrical material parameters. Parameter sweeps of the quantities marked in blue are shown in Fig. S9 in the supplementary material.

more demanding. In the scope of this tutorial, we, therefore, focus on the local parameter sensitivity at the final fit.

In previous publications on single-carrier devices and on organic as well as perovskite solar cells, we have studied the qualitative influence of the involved parameters by a systematic variation around the values from the final fit.^{19,27,60} In the present paper on OLEDs, we show the sensitivity of the electron mobility parameters $\mu_{0,n}$ and γ_n of the EML as well as the zero-field hole mobility in the NBPhen layer on the selected measurements (Fig. S9 in the supplementary material). Due to the large number of parameters, devices, and performed measurements, this will not be presented here in detail. Both EML parameters show a certain influence on one or the other experiment. Interestingly, they seem not to influence the TEL rise [Figs. S9(e) and S9(k) in the supplementary material] while both have, for example, an effect on the IV curve between 2

and 3 V [Figs. S9(a) and S9(f) in the [supplementary material](#)]. Therefore, these parameters cannot be accurately determined from a TEL rise fit alone. This finding again demonstrates how important it is to combine different measurements to be sensitive to as many parameters as possible. In Fig. S9 in the [supplementary material](#), we also show a parameter sweep of the NBPhen hole mobility. Note that this parameter was not used as a fitting parameter. A variation of ± 1 order of magnitude does not have any influence on the selected measurement techniques. One can say that we are not sensitive to this parameter, and one should, thus, not try to determine this parameter from the selected experiments.

In order to obtain a more quantitative analysis of the sensitivity with respect to the involved model parameters, we again consider the error f_i between the measured data and the simulation at N different user-defined target points [see Eq. (6)] and define the local sensitivity as

$$S_{p_j} = \sum_{i=1}^N \left(\frac{\partial f_i}{\partial p_j} \right)^2. \quad (6)$$

The calculated local sensitivity can take values between zero and infinity. The results are shown in [Fig. 11](#) and ordered from high to low.

For the three exemplary parameters discussed above, the observed high/low influence of a systematic parameter variation on the DC, AC, and transient characteristics ([Fig. S9](#) in the [supplementary material](#)) is confirmed by corresponding high/low sensitivity ([Fig. 11](#)). The NBPhen hole mobility, for example, which barely influences the electrical characteristics, can be found at the lower end of the sensitivity scale. Such parameters of “low” sensitivity cannot be determined accurately from the global fit and were, therefore, not used as a fitting parameter in the present study. For the EML electron mobility, in contrast, we observed a clear trend in the IV , C - f , G - f , and transient characteristics, and correspondingly, the sensitivity is several orders of magnitude higher. Such parameters can safely be determined from the global fit, provided that they also show a low correlation to other parameters. Even though there is no general definition of a lowest acceptable sensitivity, such a sensitivity analysis as shown in [Fig. 11](#) is highly valuable when selecting which parameters to include or exclude from a model fit.

Overall, we find that owing to the combination of four different experimental techniques and eight different devices, the model is sufficiently sensitive to all fitted parameters in [Table I](#). Since they additionally show a low mutual correlation ([Fig. 10](#)), these parameters can be reliably extracted from the fit to the experimental data.

IV. CONCLUSIONS

In this tutorial article, we presented a set of advanced DC, AC, and transient electro-optical measurement techniques for OLEDs that can be carried out with a single measurement system,²³ thus achieving highly consistent data for modeling by avoiding re-contacting the device in distinct sample holders of different setups. A step-by-step protocol of how this data should be analyzed using electro-optical device simulations was introduced. On the basis of this protocol, we showed in detail how a global fit can be obtained, which reproduces

the key measurements of multiple devices of varying layer thicknesses with one single set of model parameters. Beside material parameter extraction, an in-depth simulation study is highly valuable to understand the device physics and identify possible mechanisms that may hamper the OLED performance. In order to obtain a reliable set of model parameters, we demonstrated that it is of utmost importance to use complementary characterization techniques as well as multiple devices with systematic variations.

Combining steady-state, transient, and impedance measurements during device stressing will also help to distinguish between different degradation pathways. Qualitatively, charge transport modifications or an increase in trap states can be assessed by changes in specific measurement signals. Thanks to the comprehensive device simulation, it is possible to assign such changes to specific layers and parameters. Quantitative analysis of degradation, thus, will become feasible if device simulations are combined with different measurement techniques.

SUPPLEMENTARY MATERIAL

See the [supplementary material](#) for IV and TEL measurements of all devices, detailed determination of the relative permittivity of NPB and NBPhen, initial parameter sweeps, influence of the NPB trap parameters, simulated charge density profiles during TEL rise, local sensitivity of EML, and NBPhen mobility parameters.

ACKNOWLEDGMENTS

Paul-Anton Will and Sebastian Reineke from TU Dresden are acknowledged for providing the OLED samples. We thank Markus Regnat from ZHAW for ellipsometry measurements and Stéphane Altazin and Lieven Penninck from Fluxim for helpful discussions. This project has received funding from the European Union's Horizon 2020 Research and Innovation Program under Grant Agreement Nos. 646259 (MOSTOPHOS) and 760949 (CORNET).

REFERENCES

- ¹X. Cai and S. J. Su, *Adv. Funct. Mater.* **28**, 1 (2018).
- ²P. T. Kissinger and W. R. Heineman, *J. Chem. Educ.* **60**, 9242 (1983).
- ³A. J. Bard and L. R. Faulkner, *Electrochemical Methods*, 2nd ed. (John Wiley & Sons, Inc., 2001).
- ⁴J. Sworakowski and K. Janus, *Org. Electron. Phys. Mater. Appl.* **48**, 46 (2017).
- ⁵D. R. T. Zahn, G. N. Gavrilu, and M. Gorgoi, *Chem. Phys.* **325**, 99 (2006).
- ⁶A. Salehi, Y. Chen, X. Fu, C. Peng, and F. So, *ACS Appl. Mater. Interfaces* **10**(11), acsami.7b18514 (2018).
- ⁷A. Mikaeili, T. Matsushima, Y. Esaki, S. A. Yazdani, C. Adachi, and E. Mohajerani, *Opt. Mater.* **91**, 93 (2019).
- ⁸T. Matsushima, K. Shiomura, S. Naka, and H. Murata, *Thin Solid Films* **520**, 2283 (2012).
- ⁹Y. Esaki, T. Komino, T. Matsushima, and C. Adachi, *J. Phys. Chem. Lett.* **8**, 5891 (2017).
- ¹⁰D. Yokoyama, A. Sakaguchi, M. Suzuki, and C. Adachi, *Org. Electron. Phys. Mater. Appl.* **10**, 127 (2009).
- ¹¹M. T. Neukom, N. A. Reinke, K. A. Brossi, and B. Ruhstaller, *Proc. SPIE* **7722**, 77220V (2010).
- ¹²J. C. Blakesley, F. A. Castro, W. Kylberg, G. F. A. Dibb, C. Arantes, R. Valaski, M. Cremona, J. S. Kim, and J.-S. Kim, *Org. Electron.* **15**, 1263 (2014).
- ¹³M. T. Neukom, N. A. Reinke, and B. Ruhstaller, *Sol. Energy* **85**, 1250 (2011).

- ¹⁴J. Staudigel, M. Stöbel, F. Steuber, and J. Simmerer, *J. Appl. Phys.* **86**, 3895 (1999).
- ¹⁵M. Schober, M. Anderson, M. Thomschke, J. Widmer, M. Furno, R. Scholz, B. Lüssem, and K. Leo, *Phys. Rev. B Condens. Matter Mater. Phys.* **84**, 165326 (2011).
- ¹⁶M. Mesta, M. Carvelli, R. J. De Vries, H. Van Eersel, J. J. M. Van Der Holst, M. Schober, M. Furno, B. Lüssem, K. Leo, P. Loebel, R. Coehoorn, and P. A. Bobbert, *Nat. Mater.* **12**, 652 (2013).
- ¹⁷M. Neukom, S. Züfle, S. Jenatsch, and B. Ruhstaller, *Sci. Technol. Adv. Mater.* **19**, 291 (2018).
- ¹⁸M. T. Neukom, S. Züfle, and B. Ruhstaller, *Org. Electron.* **13**, 2910 (2012).
- ¹⁹S. Jenatsch, S. Altazin, P.-A. Will, M. T. Neukom, E. Knapp, S. Züfle, S. Lenk, S. Reineke, and B. Ruhstaller, *J. Appl. Phys.* **124**, 105501 (2018).
- ²⁰M. Regnat, K. P. Pernstich, and B. Ruhstaller, *Org. Electron.* **70**, 219 (2019).
- ²¹S. Altazin, S. Züfle, E. Knapp, C. Kirsch, T. D. Schmidt, L. Jäger, Y. Noguchi, W. Brütting, and B. Ruhstaller, *Org. Electron.* **39**, 244 (2016).
- ²²C. Peng, A. Salehi, Y. Chen, M. Danz, G. Liaptsis, and F. So, *ACS Appl. Mater. Interfaces* **9**, 41421 (2017).
- ²³Fluxim AG, Switzerland, see www.fluxim.com for Platform for all-in-one characterization (Paios).
- ²⁴A. Salehi, C. Dong, D. H. Shin, L. Zhu, C. Papa, A. Thy Bui, F. N. Castellano, and F. So, *Nat. Commun.* **10**, 2305 (2019).
- ²⁵S. L. M. Van Mensfoort and R. Coehoorn, *Phys. Rev. Lett.* **100**, 1 (2008).
- ²⁶S. Jenatsch, R. Hany, A. C. Véron, M. Neukom, S. Züfle, A. Borgschulte, B. Ruhstaller, and F. Nüesch, *J. Phys. Chem. C* **118**, 17036 (2014).
- ²⁷M. T. Neukom, A. Schiller, S. Züfle, E. Knapp, J. Ávila, D. Pérez-del-Rey, C. Dreessen, K. P. S. Zanoni, M. Sessolo, H. J. Bolink, and B. Ruhstaller, *ACS Appl. Mater. Interfaces* **11**, 23320 (2019).
- ²⁸G. Garcia-Belmonte, A. Guerrero, and J. Bisquert, *J. Phys. Chem. Lett.* **4**, 877 (2013).
- ²⁹S. Nowy, W. Ren, A. Elschner, W. Lövenich, and W. Brütting, *J. Appl. Phys.* **107**, 054501 (2010).
- ³⁰S. Züfle, S. Altazin, A. Hofmann, L. Jäger, M. T. Neukom, W. Brütting, and B. Ruhstaller, *J. Appl. Phys.* **122**, 115502 (2017).
- ³¹E. Knapp and B. Ruhstaller, *J. Appl. Phys.* **112**, 024519 (2012).
- ³²S. Nowy, W. Ren, J. Wagner, J. A. Weber, and W. Brütting, *Proc. SPIE* **7415**, 74150G (2009).
- ³³E. Knapp and B. Ruhstaller, *Appl. Phys. Lett.* **99**, 093304 (2011).
- ³⁴F. Fabregat-Santiago, G. Garcia-Belmonte, I. Mora-Sero, and J. Bisquert, *Phys. Chem. Chem. Phys.* **13**, 9083 (2011).
- ³⁵I. Mora-Seró, G. Garcia-Belmonte, P. P. Boix, M. A. Vázquez, and J. Bisquert, *Energy Environ. Sci.* **2**, 678 (2009).
- ³⁶D. J. Pinner, R. H. Friend, and N. Tessler, *J. Appl. Phys.* **86**, 5116 (1999).
- ³⁷S. Barth, P. Müller, H. Riel, P. F. Seidler, W. Rieß, H. Vestweber, and H. Bässler, *J. Appl. Phys.* **89**, 3711 (2001).
- ³⁸B. Ruhstaller, S. A. Carter, S. Barth, H. Riel, W. Riess, and J. C. Scott, *J. Appl. Phys.* **89**, 4575 (2001).
- ³⁹Q. Niu, P. W. M. Blom, F. May, P. Heimel, M. Zhang, C. Eickhoff, U. Heinemeyer, C. Lennartz, and N. I. Crăciun, *J. Appl. Phys.* **122**, 185502 (2017).
- ⁴⁰B. Ruhstaller, T. Beierlein, H. Riel, S. Karg, J. C. Scott, and W. Riess, *IEEE J. Sel. Top. Quantum Electron.* **9**, 723 (2003).
- ⁴¹S. Wehrmeister, L. Jäger, T. Wehler, A. F. Rausch, T. C. G. Reusch, T. D. Schmidt, and W. Brütting, *Phys. Rev. Appl.* **3**, 024008 (2015).
- ⁴²S. Mladenovski, S. Hofmann, S. Reineke, L. Penninck, T. Verschuere, and K. Neyts, *J. Appl. Phys.* **109**, 083114 (2011).
- ⁴³M. Regnat, K. P. Pernstich, K.-H. Kim, J.-J. Kim, F. Nüesch, and B. Ruhstaller, "Routes for efficiency enhancement in fluorescent TADF Exciplex host OLEDs gained from an electro-optical device model," *Adv. Electron. Mater.* (2019).
- ⁴⁴T. D. Schmidt, L. Jäger, Y. Noguchi, H. Ishii, and W. Brütting, *J. Appl. Phys.* **117**, 215502 (2015).
- ⁴⁵G. Juška, M. Viliūnas, K. Arlauskas, N. Nekrašas, N. Wyrsh, and L. Feitknecht, *J. Appl. Phys.* **89**, 4971 (2001).
- ⁴⁶G. Juška, K. Arlauskas, M. Viliūnas, and J. Kočka, *Phys. Rev. Lett.* **84**, 4946 (2000).
- ⁴⁷V. Kazūkauskas, A. Arlauskas, M. Pranaitis, R. Lessmann, M. Riede, and K. Leo, *Opt. Mater. (Amsterdam)* **32**, 1676 (2010).
- ⁴⁸L. Wang, S. Jenatsch, B. Ruhstaller, C. Hinderling, D. Gesevičius, R. Hany, and F. Nüesch, *Adv. Funct. Mater.* **28**, 1705724 (2018).
- ⁴⁹S. Züfle, S. Altazin, A. Hofmann, L. Jäger, M. T. Neukom, T. D. Schmidt, W. Brütting, and B. Ruhstaller, *J. Appl. Phys.* **121**, 175501 (2017).
- ⁵⁰Y. Gao, A. Pivrikas, B. Xu, Y. Liu, W. Xu, P. H. M. Van Loosdrecht, and W. Tian, *Synth. Met.* **203**, 187 (2015).
- ⁵¹O. J. Sandberg, M. Nyman, S. Dahlström, S. Sandén, B. Törngren, J. H. Smått, and R. Österbacka, *Appl. Phys. Lett.* **110**, 153504 (2017).
- ⁵²O. J. Sandberg and M. Nyman, *Org. Electron. Phys. Mater. Appl.* **64**, 97 (2019).
- ⁵³A. J. Mozer, N. S. Sariciftci, L. Lutsen, D. Vanderzande, R. Österbacka, M. Westerling, and G. Juška, *Appl. Phys. Lett.* **86**, 112104 (2005).
- ⁵⁴S. Bange, M. Schubert, and D. Neher, *Phys. Rev. B: Condens. Matter Mater. Phys.* **81**, 035209 (2010).
- ⁵⁵J. Lorrmann, B. H. Badada, O. Inganäs, V. Dyakonov, and C. Deibel, *J. Appl. Phys.* **108**, 113705 (2010).
- ⁵⁶A. Armin, G. Juska, M. Ullah, M. Velusamy, P. L. Burn, P. Meredith, and A. Pivrikas, *Adv. Energy Mater.* **4**, 1300954 (2014).
- ⁵⁷B. Ruhstaller, E. Knapp, B. Perucco, N. Reinke, D. Rezzonico, and F. Müller, in *Optoelectronic Devices and Properties*, edited by P. O. Sergiyenko (InTech, 2011).
- ⁵⁸S. Altazin, L. Penninck, and B. Ruhstaller, *Handbook of Organic Light-Emitting Diodes* (Springer Japan, Tokyo, 2018), pp. 1–22.
- ⁵⁹Fluxim AG, Switzerland, see www.fluxim.com for Simulation software Setfos (version 4.6).
- ⁶⁰R. Häusermann, E. Knapp, M. Moos, N. A. Reinke, T. Platz, and B. Ruhstaller, *J. Appl. Phys.* **106**, 104507 (2009).
- ⁶¹H. Shin, J.-H. Lee, C.-K. Moon, J.-S. Huh, B. Sim, and J.-J. Kim, in *Org. Light Emit. Mater. Devices XX*, edited by F. So, C. Adachi, and J.-J. Kim (International Society for Optics and Photonics, 2016), p. 99411X.
- ⁶²A. Salehi, S. Ho, Y. Chen, C. Peng, H. Yersin, and F. So, *Adv. Opt. Mater.* **5**, 1700197 (2017).
- ⁶³H. Nakanotani, K. Masui, J. Nishide, T. Shibata, and C. Adachi, *Sci. Rep.* **3**, 2127 (2013).
- ⁶⁴D.-S. Leem, S. O. Jung, S.-O. Kim, J.-W. Park, J. W. Kim, Y.-S. Park, Y.-H. Kim, S.-K. Kwon, and J.-J. Kim, *J. Mater. Chem.* **19**, 8824 (2009).
- ⁶⁵M. Regnat, K. P. Pernstich, S. Züfle, and B. Ruhstaller, *ACS Appl. Mater. Interfaces* **10**, 31552 (2018).
- ⁶⁶S. Gottardi, M. Barbry, R. Coehoorn, and H. Van Eersel, *Appl. Phys. Lett.* **073301**, 1 (2018).
- ⁶⁷H. Yoshida and K. Yoshizaki, *Org. Electron. Phys. Mater. Appl.* **20**, 24 (2015).
- ⁶⁸T.-Y. Chu and O.-K. Song, *Appl. Phys. Lett.* **90**, 203512 (2007).
- ⁶⁹N. B. Kotadiya, H. Lu, A. Mondal, Y. Ie, D. Andrienko, P. M. W. M. W. Blom, and G.-J. A. H. A. Wetzelaer, *Nat. Mater.* **17**, 329 (2018).
- ⁷⁰J. Li, S. C. Dong, A. Opitz, L. S. Liao, and N. Koch, *J. Mater. Chem. C* **5**, 6989 (2017).
- ⁷¹S. Naka, H. Okada, H. Onnagawa, and T. Tsutsui, *Appl. Phys. Lett.* **76**, 197 (2000).
- ⁷²S. L. M. van Mensfoort and R. Coehoorn, *Phys. Rev. B* **78**, 085207 (2008).
- ⁷³E. Knapp, R. Häusermann, H. U. Schwarzenbach, and B. Ruhstaller, *J. Appl. Phys.* **108**, 054504 (2010).
- ⁷⁴A. S. D. Sandanayaka, T. Matsushima, and C. Adachi, *J. Phys. Chem. C* **119**, 23845 (2015).
- ⁷⁵J. S. Bangsund, K. W. Hershey, and R. J. Holmes, *ACS Appl. Mater. Interfaces* **10**, 5693 (2018).
- ⁷⁶S. Jenatsch, S. Züfle, P.-A. Will, B. Blülle, M. Neukom, S. Lenk, S. Reineke, D. Braga, K. Domanski, and B. Ruhstaller, *SID Symp. Dig. Tech. Pap.* **50**, 1895 (2019).